PHYSICS

Boosting spatial and energy resolution in STM with a double-functionalized probe

Artem Odobesko[1]*, Raffael L. Klees[2,3], Felix Friedrich[1], Ewelina M. Hankiewicz[2], Matthias Bode[1,4]

The scattering of superconducting pairs by magnetic impurities on a superconducting surface leads to pairs of sharp in-gap resonances known as Yu-Shiba-Rusinov (YSR) bound states. Similar to the interference of itinerant electrons scattered by defects in normal metals, these resonances reveal a periodic texture around the magnetic impurity. The wavelength of these resonances is, however, often too short to be resolved even by methods capable of atomic resolution, i.e., scanning tunneling microscopy (STM). We combine a CO molecule with a superconducting cluster pre-attached to an STM tip to maximize both spatial and energy resolution, thus demonstrating the superior properties of such double-functionalized probes by imaging the spatial distribution of YSR states. Our approach reveals rich interference patterns of the hybridized YSR states of two Fe atoms on Nb(110), previously inaccessible with conventional STM probes. This advancement extends the capabilities of STM techniques, providing insights into superconducting phenomena at the atomic scale.

INTRODUCTION

The invention of the scanning tunneling microscope has revolutionized our understanding of materials and their properties (*1*). This progress was made possible by the capability of correlating topographic data of the sample structure being obtained by constant-current or constant-height scanning tunneling microscopy (STM) (*2*) with the data being measured by scanning tunneling spectroscopy (STS) or spin-polarized (SP)–STM. While the former is sensitive to the local density of states (LDOS) (*3*), the latter grants access to the atomic scale spin structure (*4*). However, when performed with normal metal tips, all these methods have their specific limitations, which can be overcome by purposive functionalization. The spatial resolution of topographic STM measurements can be enhanced by attaching a CO molecule to the apex of the STM probe (*5*, *6*); see red circle in Fig. 1. A superconducting (SC) probe boosts the energy resolution in STS beyond the thermal broadening limit (blue circle) (*7*), and a magnetic atom at the probe apex acts as a spin sensor in SP-STM measurements (green circle) (*8*). In particular, the advantages in the probe functionalization are not only in the improved STM and STS performance but also the fact that the probe can be sequentially prepared in a single experimental run by dressing the apex in situ for specific needs (*9*).

Enhancing probe functionalization methods can yield further advancements. The depicted intersection areas *a*-*b*-*c* in Fig. 1 illustrate the potential of double functionalization in harnessing multiple advantages simultaneously. For example, Schneider *et al.* (*10*) and Küster *et al.* (*11*) demonstrated the efficacy of combining a magnetic atom with an SC probe, considerably enhancing spin contrast at the atomic level (intersection *b* in Fig. 1) compared to bulk magnetic tips. Similarly, region *c* involves combinations with magnetic moment–bearing molecules like nickelocene (*12*, *13*), resulting in nearly 100% spin polarization and improved spatial resolution. Yet, the successful double functionalization to cover intersection area *a* remains elusive. To address this gap, we use a combination of an SC probe and a CO molecule creating a double-functionalized CO-SC probe. Leveraging improved spectroscopic and spatial resolution, we explore previously inaccessible details in the LDOS around magnetic Fe atoms on an SC Nb(110) surface. A single magnetic impurity results in a pair of particle-hole-symmetric sub-gap resonances, known as Yu-Shiba-Rusinov (YSR) bound states. The wave function of these YSR states (i) reflects the shape of the atomic orbital responsible for magnetic scattering, (ii) oscillates with the Fermi wave vector k_F, and (iii) decays with the distance r from the impurity (*14*–*16*). The decay involves two length scales: an exponential term $\propto e^{-r/\xi_0}$, governed by the SC coherence length ξ_0, and an algebraic term $\propto(k_F \cdot r)^{(1-D)/2}$ that depends on the dimension D of the system. In three-dimensional materials, the wave function diminishes rapidly primarily due to the algebraic term. This challenge persists for most elemental superconductors as the coherence length ξ_0 is much larger than the Fermi wavelength k_F^{-1}, thereby impeding direct observation of YSR wave function oscillations. Although, some observations have been successful in lower-dimensional systems or those exhibiting a strong Fermi surface nesting effect (*17*–*21*), it still remains elusive in many cases. Moreover, in the case of magnetic dimers, where more pronounced interference of YSR wave functions from individual magnetic atoms can be expected (*22*, *23*), numerous STS experiments on various SC substrates reveal only broadened initial peaks of odd and even combinations of YSR wave functions (*9*, *24*–*32*). The challenge of achieving simultaneous high spatial and spectroscopic resolution remains a limiting factor for accessing long-range oscillatory YSR interference patterns.

In this work, by using an innovative double-functionalized CO-SC probe, we detected unique interference patterns in spatially resolved differential conductance maps of the hybridized YSR states of Fe dimers. Comparing data obtained with and without additional functionalization with a CO molecule, we demonstrate a simultaneous enhancement in spatial and energy resolutions. The distinctive features in the interference maps reveal information about the anisotropy of the Fermi surface of Nb(110), which are exclusively observed when using the double-functionalized CO-SC probe. An analytical model with an

[1]Physikalisches Institut, Experimentelle Physik II, Julius-Maximilians-Universität Würzburg, Am Hubland, 97074 Würzburg, Germany. [2]Institut für Theoretische Physik und Astrophysik, Julius-Maximilians-Universität Würzburg, Am Hubland, 97074 Würzburg, Germany. [3]Institute of Physics, University of Augsburg, D-86159 Augsburg, Germany. [4]Wilhelm Conrad Röntgen-Center for Complex Material Systems (RCCM), Julius-Maximilians-Universität Würzburg, Am Hubland, 97074 Würzburg, Germany.
*Corresponding author. Email: artem.odobesko@uni-wuerzburg.de

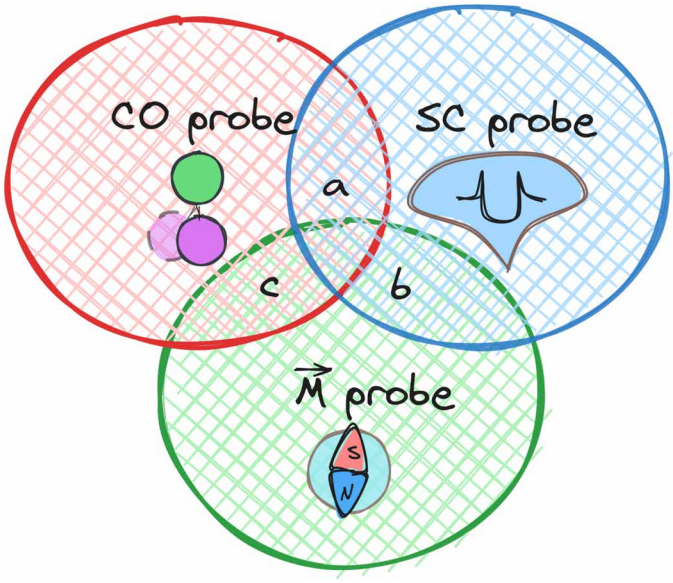

Fig. 1. Diagram displaying the three basic methods of STM, STS, and SP-STM. Their sensitivity can be enhanced by functionalization with a CO molecule, a superconducting (SC) cluster, or a magnetic atom, resulting in higher spatial resolution in topography, improved energy resolution in spectroscopy, and increased magnetic sensitivity in SP measurements, respectively. The intersection between these areas represents double-functionalization approaches.

anisotropic Fermi contour reproduces the observed interference patterns by introducing a Fermi wave vector $k_F = (9.4 \pm 1.5)\ \mathrm{nm}^{-1}$.

RESULTS

Figure 2A shows a constant-current STM image of Fe atoms deposited on a clean Nb(110) surface, taken with the double-functionalized CO-SC probe at $T = 1.4$ K. The Nb(110) surface with its lattice constant of $a_{Nb} = 3.3$Å is atomically resolved. The dark areas in Fig. 2A are contaminated with hydrogen or oxygen. Fe adatoms, visible as bright protrusions, adsorb in fourfold hollow sites of the Nb(110) lattice (*33*, *34*). Some Fe atoms spontaneously form dimers. We will focus on those Fe dimers with the shortest interatomic distance, oriented roughly along the $[1\bar{1}1]$ and $[\bar{1}\bar{1}1]$ directions, equivalent due to surface mirror symmetry. These Fe dimers exhibit energy-split YSR states, as demonstrated in previous studies (*9*).

Figure 2B shows dI/dU spectra obtained with a CO-SC probe on both the clean Nb(110) surface (dashed line) and at the central position of the Fe dimer (solid line). Tunneling from an SC probe induces a shift of all spectral features by $\Delta_{tip} \approx 1.2$ meV, marked with vertical dotted lines (*35*). Three pairs of distinct peaks are visible in the spectrum of the dimer, located at $U = \pm 2.5$, ± 2.1, and ± 1.3 mV. The inner peaks at ± 2.1 and ± 1.3 mV correspond to YSR resonances that are split within the Fe-Fe dimer due to the hybridization of single YSR states from individual Fe atoms, as extensively discussed in (*9*). The outer peaks at ± 2.5 mV partially overlap with the Nb BCS coherence peaks observed in spectrum of the clean Nb positioned at $\Delta_{tip} + \Delta_{Nb}$. Their presence on the Fe dimer suggests a second tunneling channel that directly accesses the SC substrate, bypassing YSR states within the gap (*36*). Furthermore, weak resonances at $U \approx \pm 5.3$ mV are observed, which are absent without a CO molecule at the probe apex. They correspond to the first vibrational mode of the CO molecule, which, for resonant tunneling in SC tunnel junctions, appears as peaks rather than steps in the dI/dU signal, as is the case for normal-metallic tips (*37*).

High-resolution STM imaging with CO-functionalized probes is achieved by leveraging the bending of the molecule at the probe apex due to Pauli repulsion (*6*, *38*, *39*). At close probe-sample distances, the molecule at the apex undergoes relaxation toward local minima in the interaction potential. The relaxation causes discontinuities in both the frequency shift and tunneling current signal and becomes observable in atomic force microscopy (AFM) and STM images as sharp contrast features.

In Fig. 2 (D to I), we present two sets of data measured with the CO-SC probe in a constant-current mode at various probe-sample distances above the Fe dimer. The top row represents the noncontact regime at low $I_{set} = 0.4$ nA, while the bottom row illustrates the soft-contact regime at higher $I_{set} = 1$ nA.

In case of the noncontact tunneling regime, a close-up of the topography in Fig. 2D reveals the Fe dimer in the $[1\bar{1}1]$ direction. The dimer appears as a single protrusion with a subtle elongation along its axis, while the atomic structure of the Nb(110) surface remains elusive, thus suggesting a low-resolution regime. The black dots mark the positions of the Fe atoms. Figure 2 (E and F) showcases simultaneously measured differential tunneling conductance maps, at tunneling energies aligned with the positions of high- and low-energy hybridized YSR states, respectively. In the noncontact regime, the resolution enhancement in dI/dU maps is minimal and comparable to data obtained with a single-functionalized SC-probe, as presented in (*9*). In particular, any long-range oscillatory YSR interference pattern is absent. Confirming previous observations, the high-energy YSR state at $U = -2.1$ mV displays an even symmetry, with the strongest signal centered around the dimer. Conversely, the low-energy YSR state at $U = -1.3$ mV exhibits an odd symmetry, featuring two lobes offset from the dimer center. The replicas at positive tunneling voltages are identical (see fig. S4).

The topography of the same area at a closer tip-sample distance is shown in Fig. 2G. A direct comparison between the two datasets reveals a notable improvement in spatial resolution, as the atomic resolution of the Nb surface now becomes visible, and individual Fe atoms forming the dimer are distinguishable. Notably, a similar enhancement of the spatial resolution is observed in the differential tunneling conductance maps. Even a superficial inspection of the experimental dI/dU maps reveals interference patterns that carry a much higher degree of detail compared to the data presented in Fig. 2 (E and F).

The dI/dU map of the high-energy YSR state in Fig. 2H reveals four distinguishable maxima periodically arranged in a direction perpendicular to the dimer axis. These maxima exhibit an elongated shape with the two central ones partially overlapping. This spatial arrangement aligns with the expected even symmetry shown in Fig. 2E. A very different interference pattern is observed for the low-energy YSR state, shown in Fig. 2I, revealing a sequence of arc-shaped maxima arranged along the dimer axis. Up to three maxima are observable on each side, and their intensity rapidly attenuates with increasing distance from the dimer. The arrangement of these maxima strongly suggests an odd symmetry, with a notable exception: the maximum in the center. In the case of an antisymmetric combination of the wave functions, one would anticipate a zero signal at the center of the dimer. However, the data reveal a sharp peak along the nodal plane of the dimer, in contrast to the data presented in Fig. 2F.

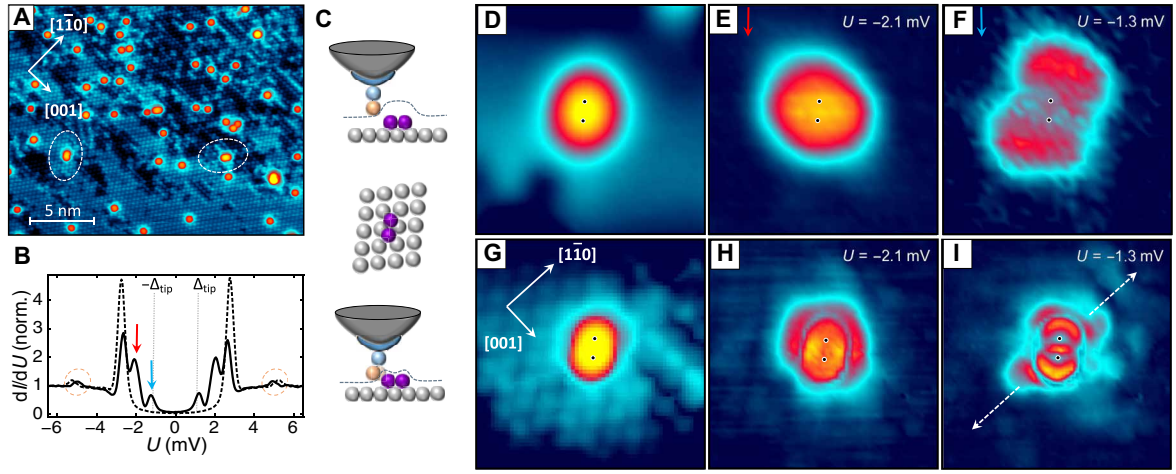

Fig. 2. Topography and density-of-states maps of Fe atoms on Nb surface. (**A**) STM topography of Fe atoms (bright protrusions) deposited on Nb(110) captured with a CO-SC probe. Two dimers along the $[1\bar{1}1]$ (left) and the $[1\bar{1}1]$ (right), highlighted with dashed ellipses, can be seen. $U_{set} = 10$ mV, $I_{set} = 2$ nA. (**B**) Single-point *dI*/*dU* spectra measured on clean Nb(110) (dashed line) and at the center of Fe dimer (solid line). The tip gap is indicated with vertical doted lines. $U_{set} = 7$ mV, $I_{set} = 0.4$ nA. (**C**) The sketches represent a CO-SC probe scanning over a magnetic Fe dimer in both noncontact tunneling regime and soft-contact tunneling regime, undergoing Pauli repulsion. (**D**) STM topography of Fe dimer along the $[1\bar{1}1]$, scale of 3 nm by 3 nm measured in noncontact tunneling regime. $U_{set} = 7$ mV, $I_{set} = 0.4$ nA. (**E**) Simultaneously measured spatial *dI*/*dU* map at the tunneling bias corresponding to the high-energy YSR state with even symmetry. (**F**) *dI*/*dU* map at the tunneling bias corresponding to the low-energy YSR state with odd symmetry. (**G** to **I**) Same as in (D) to (F) but with CO-SC probe in a soft-contact mode. $U_{set} = 7$ mV, $I_{set} = 1$ nA.

The unexpected positioning of the central maximum in the *dI*/*dU* map of Fig. 2I arises from the intricate interdependence of the tunneling conductance, which is not solely determined by the convolution of the LDOS of the tip and sample but is also influenced by the tunneling matrix elements between different orbitals. Hence, the significance of the tip tunneling orbital cannot be overstated. An accurate representation of the intrinsic spatial distribution of the sample's wave function in *dI*/*dU* maps is only achieved when using an STM tip governed by either s- or p_z-like frontier orbital, thereby maintaining an even s-type symmetry. Nevertheless, it is essential to acknowledge that CO-terminated tips, especially when the CO molecule is bent, thus inducing tunneling through the p_x and p_y orbitals as well. These orbitals carry odd p-type symmetry (*40*). As discussed in (*41*–*43*) and later shown here in the context of high-resolution imaging with CO-functionalized probe (*44*), these frontier p-type orbitals result in so-called derivative rules of the tunneling conductance maps, resulting in a contrast inversion of the intrinsic surface LDOS. Hence, both effects contribute to the measurable spatial *dI*/*dU* maps and should be appropriately taken into account.

In addition, closer inspection of the data furthermore presented in Fig. 2I (see also fig. S4 for a mirror symmetric dimer in $[1\bar{1}1]$ direction) indicates that the intensity along the arcs is not uniform but more concentrated along the direction marked by the arrows, where it experiences a weaker attenuation with distance. Comparison with the crystallographic axes reveals that, irrespective of the dimer orientation, this direction is aligned with the Nb $\langle 1\bar{1}0 \rangle$ axis. This observation strongly suggests the presence of a Fermi surface nesting with parallel flat segments of the constant-energy contour along $[1\bar{1}0]$, which provide multiple scattering vectors, resulting in the so-called "focusing effect" with a longer propagation of the YSR along this specific direction (*19*–*21*).

DISCUSSION

To rationalize our results, we model the experimental data with a simplified two-dimensional continuous model of a bare SC surface with an anisotropic stadium-shaped Fermi surface, as shown in Fig. 3A. A lattice model with a similar Fermi surface was already successfully used in (*45*). We introduce a parameter $a \in [0, k_F]$ that defines the length of the flat segments of the Fermi contour, where $a = 0$ corresponds to a circular shape with the Fermi wave vector k_F. Because the Fermi velocity points always perpendicular to the Fermi surface contour, $a > 0$ generates a focusing of the hybridized YSR-state propagation along the $[1\bar{1}0]$ direction in real space, whose strength increases with increasing a. In the following, we focus our analysis on the LDOS of the impurity-dressed substrate, keeping in mind that the experimental data obtained from STS are actually a convolution of the LDOS of the substrate and the tip. The influence of the tip orbital will be discussed further.

Following the Green's function approach described in (*21*), we model the Fe dimer by adding two magnetic impurities at an inter-impurity distance d on the bare SC substrate. We fix $d = (2.66 \pm 0.18)$ Å to the average between the two extremes Fe and Nb with nearest-neighbor distances of 2.48 and 2.85 Å, as discussed in the Supplementary Materials. We also account for the epitaxial strain between the Fe dimer and the Nb(110) substrate, where the axis of the Fe dimer is rotated clockwise by an angle of 4° with respect to the $[1\bar{1}1]$ direction. For simplicity, these impurities are assumed to be identical and described by a semiclassical Shiba model (*15*) with an onsite energy U and an exchange coupling J.

The Fermi momentum k_F is chosen to match the oscillation pattern in the experimental data. We find a good match between our theoretical model with a simplified shape of the Fermi contour and the experimental data for $k_F = \frac{2.5}{d} \approx (9.4 \pm 1.5)\ \mathrm{nm}^{-1}$, see fig. S6. Unexpectedly, this value for k_F estimated for Fe impurities on

Nb(110) is almost two times larger than the one obtained for Mn on Nb(110) (*46*). It is important to note that k_F for Fe atoms is estimated for YSR states, which correspond to scattering channels related to the d_{z^2} orbital, whereas for Mn k_F is obtained for the d_{yz} orbital (*46*). We speculate that the relatively large difference in the effective Fermi wave length k_F for screening magnetic impurities is caused by the fact that the d_{yz} states of Mn and the d_{z^2} states of Fe hybridize with very different bands of the Nb Fermi surface. Further ab initio calculations would be desirable to clarify this issue.

In Fig. 3B, we show the resulting LDOS at one of the impurity sites, which shows two pairs of hybridized YSR bound states at the energies $E_{S,n}$ (n = 1,2,3, and 4) with $E_{S,4} = -E_{S,1} \approx 0.69\ \Delta_{Nb}$ and $E_{S,3} = -E_{S,2} \approx 0.15\ \Delta_{Nb}$. The parameters U and J are chosen such that the energy difference of the positive and negative pair is $\Delta E = |E_{S,4}| - |E_{S,3}| \approx 0.54\ \Delta_{Nb}$, which corresponds to the experimentally observed value ≈0.8 meV.

In the first row in Fig. 3C, we show the spatial behavior of the LDOS, i.e., the wave function $|\psi_n|^2$, of the four YSR bound states. While the high-energy pair of YSR states shows even symmetry with a finite value at the origin, the low-energy pair shows odd symmetry and vanishes at the origin. The calculated LDOS maps are in good agreement with the tunneling conductance maps observed experimentally. In particular, the LDOS map at the energy $E_{S,1}$ ($E_{S,2}$) qualitatively reproduces the high (low) LDOS in the nodal plane for the even-symmetric (odd-symmetric) YSR state at $U = -2.1$ mV ($U = -1.3$ mV). Furthermore, the model reproduces the focusing effect along the $[1\bar{1}0]$ direction, marked with arrows in Fig. 3C. Because the theoretical model is two-dimensional, the attenuation of YSR wave function is strongly reduced, and an additional set of maxima in the other direction is also observed. They arise from the remaining circular segment of the Fermi contour and their direction rotates with the orientation of the dimer, whereas the "focusing" direction is independent of the dimer orientation and always directed along $[1\bar{1}0]$. However, the experimental measurement data in Fig. 2I show a peak at the origin, which we attribute to tunneling through $p_{x,y}$ orbitals of the CO molecule at the tip apex. To model the measurement of the differential conductance using STM tips with non-isotropic orbitals, i.e., beyond the s orbital, one needs to take into account the shape of the tip orbital wave functions and their spatial overlap with the substrate YSR bound state wave function. This results in different transition matrix elements for tunnel processes through different orbitals, which result in so-called derivative rules (*41*–*43*). In particular, tunneling through p_α orbitals ($\alpha = x$, y, and z) leads to transition matrix elements proportional to $|\partial_\alpha \psi_n|^2$. Because of the uncertain and probably stochastically fluctuating azimuthal alignment of the p_x and p_y orbitals of the CO molecule with respect to the Fe dimer in a soft-contact regime, we assume that tunneling occurs equally through both orbitals. Consequently, the only measurable quantity becomes the gradient of the wave function in the xy plane, represented as $|\nabla \psi_n|^2$ and as depicted in the second row of Fig. 3C. Here, the gradients of the odd YSR states show a peak in the center (more pronounced in the second plot), while the gradients of the YSR states with even symmetry vanish at the origin.

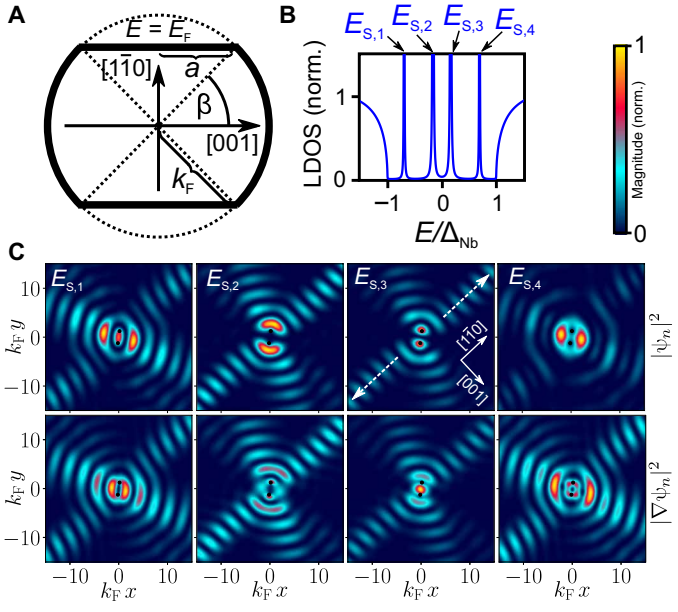

Fig. 3. Fermi surface model and resulting density of state. (**A**) Sketch of the stadium-shaped Fermi surface at the Fermi energy $E_F = 0$. $a \in [0, k_F]$ and the angle $\beta = \arccos(a/k_F)$ define the regions with flat segments, where $a = 0$ corresponds to a circular Fermi surface with radius $k_F > 0$ and $\beta = \pi/2$. (**B**) LDOS at the impurity position $r = r_1$ normalized to its large-energy value at $E = 10^3 \Delta_{Nb}$ for a pair of magnetic impurities located at $r_{1,2}$. There are two pairs of YSR states with energies $E_{S,4} = -E_{S,1} \approx \pm 0.69\ \Delta_{Nb}$ and $E_{S,3} = -E_{S,2} \approx \pm 0.15\ \Delta_{Nb}$. (**C**) Surface LDOS $|\psi_n|^2$ (first row), gradient $|\nabla \psi_n|^2$ (second row). The plots are normalized to their maximal value. Black dots represent the locations of the individual magnetic impurities. Data were rotated to fit the orientation in Fig. 2. Parameters for (B) and (C): $a = 0.6\ k_F$, $\xi_0 = 100/k_F$, $k_F = 2.5/d$, $J = -0.82/N_0$, and $U = 0.70/N_0$, where N_0 is the normal-state density of states at the Fermi energy.

Moreover, as detailed in the Supplementary Materials, our theoretical framework anticipates an energy-dependent phase shift between electron-like and hole-like YSR states, arising from the counter movement of electrons and holes, observed in (*17*). This phenomenon is distinctly evident in Fig. 3C, illustrating the difference in spatial distribution between YSR states with positive and negative energies. However, our observed tunneling conductance maps do not show such a phase variation, likely due to the combined influence of p_z and $p_{x,y}$ orbitals, which mixes and obscures these effects.

In conclusion, our findings demonstrate the advantages of double-functionalized STM tips, comprising an SC cluster and an additional CO molecule attached to it, simultaneously maximizing energy resolution and substantially enhancing spatial resolution. We have shown that, in the soft-contact tunneling regime, the bending of the CO molecule at the tip apex leads to an increase in spatial contrast in spectroscopy, which is akin to effects observed in high-resolution STM/AFM topography. This also results in additional tunneling through $p_{x,y}$ orbitals, thus yielding a signal proportional to the square of the sample wave function gradient. This further enhances spatial resolution but introduces symmetry alterations in observed features. An STM equipped with such a double-functionalized probe tips affords unique access to the fast attenuating wave functions of YSR bound states in bulk three-dimensional superconductor. Furthermore, the CO-SC probe's potential in exploring unconventional superconductivity such as odd frequency and triplet pairing (e.g., p-wave), as discussed in (*47*), paves the way for future research, amplifying its capability to investigating magnetic chains with Majorana end states and other atomic-scale quantum phenomena.

METHODS

The experiments are performed in a homebuilt low-temperature STM at a base temperature of 1.4 K. The Nb(110) surface is cleaned by a series of high-temperature flashes (*48*). Fe atoms are deposited in situ onto the Nb substrate at a temperature of 4.2 K. To get an SC probe, an electrochemically etched W tip was brought in contact with the Nb crystal, thus creating a Nb cluster on the tip apex. CO molecules were picked up from a clean Cu(001) surface using the procedure described in (*9*). The resulting double-functionalized tips exhibit an SC gap Δ_{tip}, which corresponds to about 70 to 90% of the bulk Nb value (*49*). The presence of an SC gap in the LDOS of the tip causes a corresponding shift of the sample's LDOS features in the conductance spectra by Δ_{tip}. The experimental data are obtained within the tunneling regime, where tunnel resistances $R_{tun} > 10^6$ ohms. This ensures that the tunneling current is predominantly governed by single-electron tunneling event rather than Andreev reflections, observed in both noncontact and contact regimes (*50*–*53*). All spectroscopic measurements are performed with a modulation voltage of 0.1 mV at a frequency of 890 Hz.

Supplementary Materials

This PDF file includes:

Supplementary Text
Figs. S1 to S6

REFERENCES AND NOTES

1. F. Besenbacher, Scanning tunnelling microscopy studies of metal surfaces. *Rep. Prog. Phys.* **59**, 1737–1802 (1996).
2. J. Tersoff, D. R. Hamann, Theory and application for the scanning tunneling microscope. *Phys. Rev. Lett.* **50**, 1998–2001 (1983).
3. J. Tersoff, D. R. Hamann, Theory of the scanning tunneling microscope. *Phys. Rev. B* **31**, 805–813 (1985).
4. M. Bode, Spin-polarized scanning tunnelling microscopy. *Rep. Prog. Phys.* **66**, 523–582 (2003).
5. L. Gross, F. Mohn, N. Moll, P. Liljeroth, G. Meyer, The chemical structure of a molecule resolved by atomic force microscopy. *Science* **325**, 1110–1114 (2009).
6. C. Weiss, C. Wagner, C. Kleimann, M. Rohlfing, F. S. Tautz, R. Temirov, Imaging Pauli repulsion in scanning tunneling microscopy. *Phys. Rev. Lett.* **105**, 086103 (2010).
7. S. H. Pan, E. W. Hudson, J. C. Davis, Vacuum tunneling of superconducting quasiparticles from atomically sharp scanning tunneling microscope tips. *Appl. Phys. Lett.* **73**, 2992–2994 (1998).
8. S. Loth, C. P. Lutz, A. J. Heinrich, Spin-polarized spin excitation spectroscopy. *New J. Phys.* **12**, 125021 (2010).
9. F. Friedrich, R. Boshuis, M. Bode, A. Odobesko, Coupling of Yu-Shiba-Rusinov states in one-dimensional chains of Fe atoms on Nb(110). *Phys. Rev. B* **103**, 235437 (2021).
10. L. Schneider, P. Beck, J. Wiebe, R. Wiesendanger, Atomic-scale spin-polarization maps using functionalized superconducting probes. *Sci. Adv.* **7**, eabd7302 (2021).
11. F. Küster, S. Das, S. S. P. Parkin, P. Sessi, Yu-Shiba-Rusinov tips: Imaging spins at the atomic scale with full magnetic sensitivity. arXiv:2307.09534 (2013).
12. G. Czap, P. J. Wagner, F. Xue, L. Gu, J. Li, J. Yao, R. Wu, W. Ho, Probing and imaging spin interactions with a magnetic single-molecule sensor. *Science* **364**, 670–673 (2019).
13. C. Mier, B. Verlhac, L. Garnier, R. Robles, L. Limot, N. Lorente, D.-J. Choi, Super-conducting scanning tunneling microscope tip to reveal sub-millielectronvolt magnetic energy variations on surfaces. *J. Phys. Chem. Lett.* **12**, 2983–2989 (2021).
14. L. Yu, Bound state in superconductors with paramagnetic impurities. *Acta Phys. Sin.* **21**, 75 (1965).
15. H. Shiba, Classical spins in superconductors. *Prog. Theor. Phys.* **40**, 435–451 (1968).
16. A. I. Rusinov, Superconcductivity near a paramagnetic impurity. *Zh. Eksp. Teor. Fiz. Pisma Red.* **9**, 146–149 (1968).
17. G. C. Ménard, S. Guissart, C. Brun, S. Pons, V. S. Stolyarov, F. Debontridder, M. V. Leclerc, E. Janod, L. Cario, D. Roditchev, P. Simon, T. Cren, Coherent long-range magnetic bound states in a superconductor. *Nat Phys.* **11**, 1013–1016 (2015).
18. E. Liebhaber, E. Liebhaber, S. A. González, R. Baba, G. Reecht, B. W. Heinrich, S. Rohlf, K. Rossnagel, F. von Oppen, K. J. Franke, Yu-Shiba-Rusinov states in the charge-density modulated superconductor $NbSe_2$. *Nano Lett.* **20**, 339–344 (2020).
19. M. Ruby, Y. Peng, F. von Oppen, B. W. Heinrich, K. J. Franke, Orbital picture of Yu-Shiba-Rusinov multiplets. *Phys. Rev. Lett.* **117**, 186801 (2016).
20. H. Kim, L. Rózsa, D. Schreyer, E. Simon, R. Wiesendanger, Long-range focusing of magnetic bound states in superconducting lanthanum. *Nat. Commun.* **11**, 4573 (2020).
21. J. Ortuzar, S. Trivini, M. Alvarado, M. Rouco, J. Zaldivar, A. L. Yeyati, J. I. Pascual, F. S. Bergeret, Yu-Shiba-Rusinov states in two-dimensional superconductors with arbitrary Fermi contours. *Phys. Rev. B* **105**, 245403 (2022).
22. M. E. Flatté, D. E. Reynolds, Local spectrum of a superconductor as a probe of interactions between magnetic impurities. *Phys. Rev. B* **61**, 14810 (2000).
23. D. K. Morr, N. A. Stavropoulos, Quantum interference between impurities: Creating novel many-body states in s-wave superconductors. *Phys. Rev. B* **67**, 020502 (2003).
24. S.-H. Ji, T. Zhang, Y.-S. Fu, X. Chen, X.-C. Ma, J. Li, W.-H. Duan, J.-F. Jia, Q.-K. Xue, High-resolution scanning tunneling spectroscopy of magnetic impurity induced bound states in the superconducting gap of Pb thin films. *Phys. Rev. Lett.* **100**, 226801 (2008).
25. M. Ruby, B. W. Heinrich, Y. Peng, F. von Oppen, K. J. Franke, Wave-function hybridization in Yu-Shiba-Rusinov dimers. *Phys. Rev. Lett.* **120**, 156803 (2018).
26. T. Meng, J. Klinovaja, S. Hoffman, P. Simon, D. Loss, Superconducting gap renormalization around two magnetic impurities: From Shiba to Andreev bound states. *Phys. Rev. B* **92**, 064503 (2015).
27. S. Kezilebieke, M. Dvorak, T. Ojanen, P. Liljeroth, Coupled Yu-Shiba-Rusinov states in molecular dimers on $NbSe_2$. *Nano Lett.* **18**, 2311–2315 (2018).
28. D.-J. Choi, D.-J. Choi, C. G. Fernández, E. Herrera, C. Rubio-Verdú, M. M. Ugeda, I. Guillamón, H. Suderow, J. I. Pascual, N. Lorente, Influence of magnetic ordering between Cr adatoms on the Yu-Shiba-Rusinov sates of the β−Bi_2 Pd superconductor. *Phys. Rev. Lett.* **120**, 167001 (2018).
29. Y. Kim, J. Zhang, E. Rossi, R. M. Lutchyn, Impurity-induced bound states in superconductors with spin-orbit coupling. *Phys. Rev. Lett.* **114**, 236804 (2015).
30. H. Ding, Y. Hu, M. T. Randeria, S. Hoffman, O. Deb, J. Klinovaja, D. Loss, A. Yazdani, Tuning interactions between spins in a superconductor. *Proc. Natl. Acad. Sci. U.S.A.* **118**, e2024837118 (2021).
31. F. Küster, S. Brinker, S. Lounis, S. S. P. Parkin, P. Sessi, Long range and highly tunable interaction between local spins coupled to a superconducting condensate. *Nat. Commun.* **12**, 6722 (2021).
32. P. Beck, L. Schneider, L. Rózsa, K. Palotás, A. Lászlóffy, L. Szunyogh, J. Wiebe, R. Wiesendanger, Spin-orbit coupling induced splitting of Yu-Shiba-Rusinov states in antiferromagnetic dimers. *Nat. Commun.* **12**, 2040 (2021).
33. F. Küster, A. M. Montero, F. S. M. Guimarães, S. Brinker, S. Lounis, S. S. P. Parkin, P. Sessi, Correlating Josephson supercurrents and Shiba states in quantum spins unconventionally coupled to superconductors. *Nat. Commun.* **12**, 1108 (2021).
34. A. Odobesko, D. Di Sante, A. Kowalski, S. Wilfert, F. Friedrich, R. Thomale, G. Sangiovanni, M. Bode, Observation of tunable single-atom Yu-Shiba-Rusinov states. *Phys. Rev. B* **102**, 174504 (2020).
35. K. J. Franke, G. Schulze, J. I. Pascual, Competition of superconducting phenomena and kondo screening at the nanoscale. *Science* **332**, 940–944 (2011).
36. H. Huang, R. Drost, J. Senkpiel, C. Padurariu, B. Kubala, A. L. Yeyati, J. C. Cuevas, J. Ankerhold, K. Kern, C. R. Ast, Quantum phase transitions and the role of impurity-substrate hybridization in Yu-Shiba-Rusinov states. *Common. Phys. Ther.* **3**, 199 (2020).
37. J. Homberg, A. Weismann, T. Markussen, R. Bernd, Resonance-enhanced vibrational spectroscopy of molecules on a superconductor. *Phys. Rev. Lett.* **129**, 116801 (2022).
38. P. Hapala, G. Kichin, C. Wagner, F. S. Tautz, R. Temirov, P. Jelínek, Mechanism of high-resolution STM/AFM imaging with functionalized tips. *Phys. Rev. B* **90**, 085421 (2014).
39. R. Temirov, F. S. Tautz, "Scanning tunnelling microscopy with single molecule force sensors" in *Noncontact Atomic Force Microscopy* (Springer, 2015), pp. 275–301.
40. M. Paulsson, T. Frederiksen, H. Ueba, N. Lorente, M. Brandbyge, Unified description of inelastic propensity rules for electron transport through nanoscale junctions. *Phys. Rev. Lett.* **100**, 226604 (2008).
41. C. Julian Chen, Origin of atomic resolution on metal surfaces in scanning tunneling microscopy. *Phys. Rev. Lett.* **65**, 448–451 (1990).
42. C. Julian Chen, Tunneling matrix elements in three-dimensional space: The derivative rule and the sum rule. *Phys. Rev. B Condens Matter* **42**, 8841–8857 (1990).
43. C. Julian Chen, Microscopic view of scanning tunneling microscopy. *J. Vac. Sci Technol. A* **9**, 44–50 (1991).
44. L. Gross, N. Moll, F. Mohn, A. Curioni, G. Meyer, F. Hanke, M. Persson, High-resolution molecular orbital imaging using a p-Wave STM tip. *Phys. Rev. Lett.* **107**, 086101 (2011).
45. A. Odobesko, F. Friedrich, S.-B. Zhang, S. Haldar, S. Heinze, B. Trauzettel, M. Bode, Anisotropic vortices on superconducting Nb(110). *Phys. Rev. B* **102**, 174502 (2020).
46. L. Schneider, P. Beck, J. Neuhaus-Steinmetz, L. Rózsa, T. Posske, J. Wiebe, R. Wiesendanger, Precursors of Majorana modes and their length-dependent energy oscillations probed at both ends of atomic Shiba chains. *Nat. Nanotechnol.* **17**, 384–389 (2022).

47. O. Kashuba, B. Sothmann, P. Burset, B. Trauzettel, Majorana STM as a perfect detector of odd-frequency superconductivity. *Phys. Rev. B* **95**, 174516 (2017).
48. A. B. Odobesko, S. Haldar, S. Wilfert, J. Hagen, J. Jung, N. Schmidt, P. Sessi, M. Vogt, S. Heinze, M. Bode, Preparation and electronic properties of clean superconducting Nb(110) surfaces. *Phys. Rev. B* **99**, 115437 (2019).
49. S. Bose, P. Raychaudhuri, R. Banerjee, P. Vasa, P. Ayyub, Mechanism of the size dependence of the superconducting transition of nanostructured Nb. *Phys. Rev. Lett.* **95**, 147003 (2005).
50. M. Ternes, W.-D. Schneider, J.-C. Cuevas, C. P. Lutz, C. F. Hirjibehedin, A. J. Heinrich, Subgap structure in asymmetric superconducting tunnel junctions. *Phys. Rev. B* **74**, 132501 (2006).
51. M. Ruby, F. Pientka, Y. Peng, F. von Oppen, B. W. Heinrich, K. J. Franke, Tunneling processes into localized subgap states in superconductors. *Phys. Rev. Lett.* **115**, 087001 (2015).
52. A. Villas, R. L. Klees, H. Huang, C. R. Ast, G. Rastelli, W. Belzig, J. C. Cuevas, Interplay between Yu-Shiba-Rusinov states and multiple Andreev reflections. *Phys. Rev. B* **101**, 235445 (2020).
53. A. Villas, R. L. Klees, G. Morrás, H. Huang, C. R. Ast, G. Rastelli, W. Belzig, J. C. Cuevas, Tunneling processes between Yu-Shiba-Rusinov bound states. *Phys. Rev. B* **103**, 155407 (2021).

Acknowledgments: R.L.K. acknowledges discussions with J.-C. Cuevas and D. Gresta. **Funding:** This work was supported by Deutsche Forschungsgemeinschaft (DFG; German Research Foundation) through SFB 1170 (project C02 and BO3). We also acknowledge financial support by DFG under Germany's Excellence Strategy through Würzburg-Dresden Cluster of Excellence on Complexity and Topology in Quantum Matter–ct.qmat (EXC 2147, project ID 390858490). **Author contributions:** A.O. and F.F. conducted the experiments and analyzed the data. R.L.K. carried out the simulations and calculations. A.O. conceived and directed the study. M.B. and E.M.H. supervised the project. A.O. and R.L.K. wrote the initial version of the manuscript. All authors discussed the results and their interpretation. A.O., R.L.K., F.F., and M.B. contributed to the manuscript. **Competing interests:** The authors declare that they have no competing interests. **Data and materials availability:** All data needed to evaluate the conclusions in the paper are present in the paper and/or the Supplementary Materials.

Submitted 27 May 2024
Accepted 24 July 2024
Published 28 August 2024
10.1126/sciadv.adq6975